ORIGINAL PAPER

physica status solidi
www.pss-b.com
Check for updates

Insulating State in Low-Disorder Graphene Nanoribbons

Alexander Epping, Christian Volk, Frederic Buckstegge, Kenji Watanabe,
Takashi Taniguchi, and Christoph Stampfer*

Quantum transport measurements on etched graphene nanoribbons encapsulated in hexagonal boron nitride (hBN) are reported. At zero magnetic field, the devices behave qualitatively very similar to those reported for graphene nanoribbons on SiO_2 or hBN, but exhibit a considerably smaller transport gap. At magnetic fields of around 3 T, the transport behavior changes significantly and is dominated by a much larger energy gap induced by electron–electron interactions which completely suppress the transport. This energy gap increases with a slope in the order of 3–4 meV T^{-1}, reaching values of up to 30 meV at 9 T.

1. Introduction

Graphene nanoribbons offer an interesting field for studying mesoscopic physics at the nanoscale by combining size confinement effects and the Dirac fermion nature of electrons in graphene.[1–3] Especially, electron–electron interaction in graphene nanoribbons has been studied theoretically to quite some extent.[4–10] In particular, the presence of a magnetic field gives rise to a number of transport phenomena unique to Dirac fermions. For example, high-quality graphene has already shown anomalous patterns in the magnetoconductance called Hofstadter's butterfly due to the moiré superlattice of graphene/hexagonal boron nitride (hBN) heterostructures[11,12] or quantum Hall ferromagnetism at the Dirac point.[13–16] The latter has also been realized in high-mobility suspended graphene

nanoribbons[17] although they suffer from the limited control in the fabrication process.[18] Additionally, these devices exhibit a poor gate tunability. To date, in substrate-supported graphene nanostructures, the disordered potential landscape controls the transport properties.[19–25] An alternative way to achieve very high electronic quality is placing graphene on hBN, which can significantly reduce the disorder potential.[26–30] However, in nanostructures, the contribution of edge disorder to the overall disorder remains significant.[31,32] In addition to the remaining substrate and edge-induced disorder, surface contaminations, e.g., lithography residues, have to be considered.[33] A step toward further reducing this type of disorder is to encapsulate graphene in hBN,[28] which prevents process-induced contaminations on the graphene flake, although the edges are still exposed. This results in substrate-supported devices with reproducibly high electronic quality and enables the observation of quantum phenomena such as quantized conductance in submicron-structured graphene constrictions.[34,35]

In this work, we report on low-temperature transport measurements of nanostructured graphene ribbons fully encapsulated in hBN. We characterize the transport properties of the devices at zero magnetic field as well as in the presence of a finite perpendicular magnetic field. We show that at low magnetic fields (including zero), the encapsulated nanoribbon devices exhibit the typical behavior of disordered ribbons. However, at moderate magnetic fields ($\approx$3 T), an insulating state emerges similar to that observed in high-mobility graphene,[13–16] where a gap opens due to the valley symmetry breaking induced by the perpendicular magnetic field.

A. Epping, Dr. C. Volk,[+] F. Buckstegge, Prof. C. Stampfer
JARA-FIT and 2nd Institute of Physics
RWTH Aachen University
Aachen 52074, Germany
E-mail: stampfer@physik.rwth-aachen.de

A. Epping, Dr. C. Volk, Prof. C. Stampfer
Peter Grünberg Institute (PGI-9)
Forschungszentrum Jülich
52425 Jülich, Germany

Dr. K. Watanabe, Dr. T. Taniguchi
Research Center for Functional Materials
National Institute for Materials Science
1-1 Namiki, Tsukuba 305-0044, Japan

The ORCID identification number(s) for the author(s) of this article can be found under https://doi.org/10.1002/pssb.201900269.

[+]Present address: QuTech and Kavli Institute of Nanoscience,
TU Delft, Delft, GA 2600, The Netherlands

2. Fabrication

The device fabrication was based on mechanical exfoliation of graphene and encapsulating it between two exfoliated hBN flakes via a well-established dry transfer method,[28] preventing the graphene from coming into contact with resist or organic solvents. The heterostructures were deposited on Si^{++}/SiO_2 substrates, providing the devices a back gate (BG) (see **Figure 1**a,b). To ensure high quality of the samples with a low amount of strain fluctuations,[36] each transferred heterostructure was investigated by spatially resolved Raman spectroscopy prior to the structuring. Areas with a small ($<20\,cm^{-1}$) full width at half maximum (FWHM) of the Raman 2D line and low variations were chosen for the device. A representative Raman map of the FWHM of the Raman 2D line is shown in Figure 1b and a corresponding Raman spectrum is presented in Figure 1c, see highlighted point in Figure 1b. In comparison, the FWHM of the 2D line on SiO_2

ADVANCED
SCIENCE NEWS
www.advancedsciencenews.com

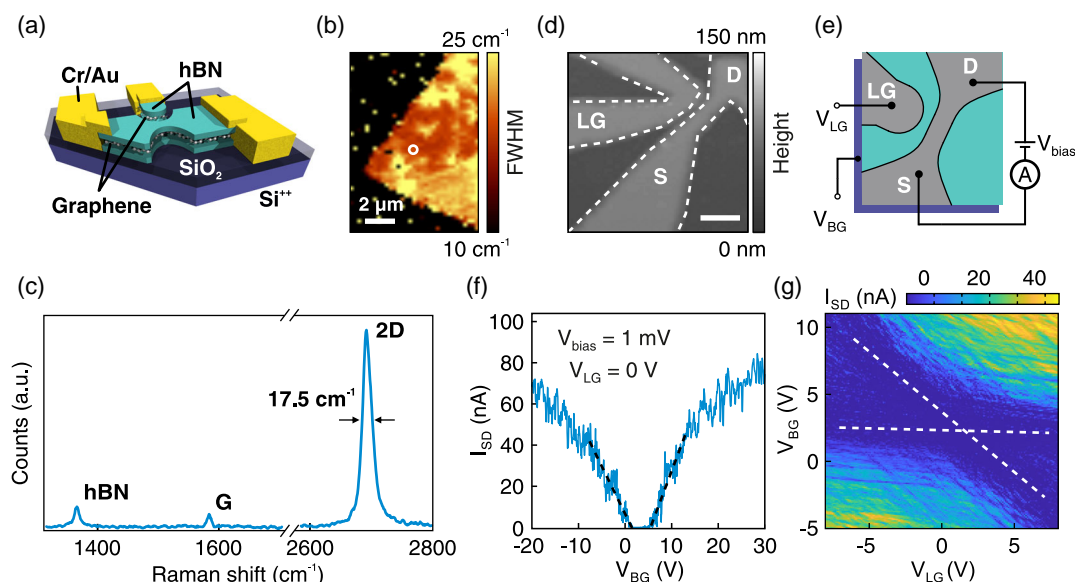physica
status
solidi b
www.pss-b.com

Figure 1. a) Schematic of the heterostructure including 1D contacts and the highly doped silicon BG. b) Map of the FWHM of the Raman 2D line before device fabrication. The circle highlights the position of the Raman spectrum shown in panel (c). c) Raman spectrum showing the individual Raman peaks of hBN and graphene. d) Atomic force micrograph of device D2. The scale bar corresponds to 150 nm. e) Illustration of the measurement configuration. The chemical potential is locally adjusted by the lateral gate (LG), while the Fermi level of the whole sample is tuned by the back gate (BG). f) Source-drain current I_{SD} as a function of BG voltage V_{BG} for a fixed bias $V_{bias} = 1$ mV and the lateral (side) gate voltage $V_{LG} = 0$ V of a nanoribbon with a width of 40 nm and a length of 150 nm. g) I_{SD} as a function of V_{BG} and V_{LG} of the same device. The transport gap (dark region) can be tuned by V_{BG} and V_{LG}. The source/drain regions are influenced only by the BG, while the region of the nanoribbon is tuned by both gates (see white dashed lines). All data taken from device D2. For similar data for device D1, see Figure S1, Supporting Information.

was typically above 30 cm^{-1}.[37] Electron beam lithography (EBL), deposition of an aluminum hard mask (20 nm), and reactive ion etching with a SF$_6$/O$_2$ plasma were used to structure the heterostructure into the desired shape. The resulting nanoribbons were then contacted in a second EBL step and subsequent metal evaporation of Cr/Au (5/75 nm). We investigated two devices (D1 and D2) based on nanoribbons with a width of around 35 (device D1) and 40 nm (device D2) and a length of 100 and 150 nm, respectively. Figure 1e shows an illustration of the measurement configuration. We performed two-terminal conductance measurements where the bias voltage was applied between the source (S) and drain (D) contacts. The charge carrier density could be tuned locally by a lateral gate (LG) based on graphene, which had a distance of around 10 nm to the nanoribbon. Globally, the Fermi level can be adjusted by the BG. All transport measurements were performed at $T \approx 30$ mK.

3. Device Characterization

In Figure 1f, we show the source-drain current I_{SD} as a function of the applied BG voltage V_{BG} through device D2 for a fixed bias $V_{bias} = 1$ mV and an LG voltage of 0 V. The region of suppressed current, commonly called transport gap ΔV_{BG}, is estimated by the distance between the intersection points of a linear approximation of the BG characteristic outside the gap region with zero I_{SD} as depicted in Figure 1f. The transport gap arises due to statistical Coulomb blockade in the nanoribbon, where the gap is related to the tunneling of electrons through charged islands and localized states in the ribbon, which result from both bulk and edge disorder.[19,20] While bulk disorder can be strongly reduced when using hBN as the substrate material,[26–30] edge disorder, the dominating disorder in nanostructured graphene devices, remains nearly unaffected.[31,32] Overall, this results in a slightly reduced disorder potential, thus reducing the transport gap. With the described method, we extract $\Delta V_{BG} = 4.5$ V, which is smaller than that reported for graphene nanoribbons of a similar size on SiO$_2$[38–41] or hBN.[32] Additionally, the charge neutrality point is close to $V_{BG} = 0$ V. Both results indicate a low residual doping of the sample and a reduced amount of disorder compared to such small structures fabricated on SiO$_2$ or without encapsulation in hBN. Device D1 shows a very similar behavior (see also Figure S1a, Supporting Information). Fixing V_{BG} inside the transport gap enables us to observe Coulomb peaks due to resonant tunneling through a network of charge islands[19] (see e.g., the $B = 0$ T trace in **Figure 2**d). To study the characteristic of the device in more detail, we investigated the dependence of I_{SD} on the LG with respect to V_{BG}. In Figure 1g, we show I_{SD} as a function of V_{BG} and V_{LG} at fixed $V_{bias} = 1$ mV. The dark region denotes the transport gap that can be tuned by both the BG and (partly) by the LG. Two different slopes marked by the white dashed lines can be identified, originating from tuning different regions of the device. The nanoribbon region is tuned by both gates, whereas the leads (source/drain contacts) are mostly independent of the voltage applied to the LG. Similar measurements were performed for both devices and resulted in a typical relative lever arm of $\alpha_{BG/LG} \approx 0.9$ to tune the transport gap, which is comparable to previous studies.[19]
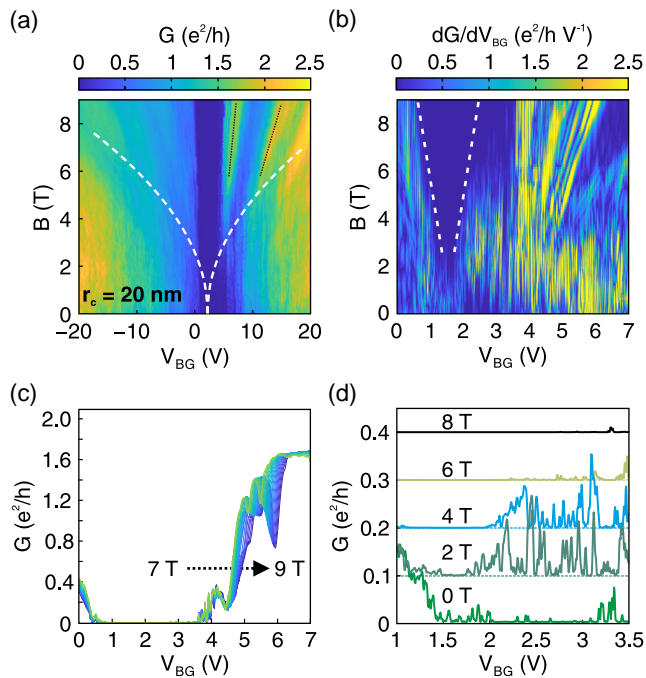
Figure 2. a) Conductance G of the 40 nm wide ribbon as a function of V_{BG} and the magnetic field B with $V_{LG} = 0$ V. The white dashed lines correspond to a cyclotron radius of $r_c = 20$ nm. b) Transconductance dG/dV_{BG} as a function of V_{BG} and the magnetic field B at $V_{LG} = 0$ V. The white dashed lines mark a region of suppressed conductance that evolves with increasing magnetic field. c) Conductance G as a function of V_{BG} between $B = 7$ and 9 T in steps of 100 mT. d) G as a function of V_{BG} for $B = 0$, 2, 4, 6, and 8 T between $V_{BG} = 1$ V and $V_{BG} = 3.5$ V. Each trace is offset by 0.1 $e^2\,h^{-1}$ for clarity. All data taken from device D2.

4. Magnetotransport

We have thus far shown that our devices behave qualitatively very similar to etched graphene nanoribbons on SiO_2 or hBN, although the transport gap is considerably smaller. We now focus on magnetotransport properties. In Figure 2a, we show the conductance G of device D2 as a function of V_{BG} and the perpendicular magnetic field B with $V_{LG} = 0$ V. Outside the transport gap, we observe features, which move linearly with increasing B-field and can be related to Landau level quantization, i.e., to quantum Hall edge states (see white dashed lines in Figure 2a). Consistently, these features are only visible once the cyclotron radius is below half of the nanoribbon width ($r_c < w/2$, white dashed lines in Figure 2a), which corresponds to the requirement for having edge channel transport through the nanoribbon. The cyclotron radius is given by $r_c = \hbar\sqrt{\pi n}/(eB)$, where $n = \alpha(V_{BG} - V_{BG}^0)$ is the charge carrier density, α is the lever arm (see below), and V_{BG}^0 is the charge neutrality point. A quantum Hall plateau can, for example, be seen on the electron side above 6 T (see also Figure 2b around $V_{BG} \approx 6$ V and Figure S2, Supporting Information). The quantum Hall plateau becomes more apparent in Figure 2c where we show the conductance G as a function of V_{BG} for magnetic fields between 7 and 9 T in steps of 100 mT. Above $V_{BG} = 6$ V, the traces form a nearly perfect plateau. Due to the two-terminal configuration, we can

only assume a filling factor of $\nu = 2$, which would correspond to a lever arm of $\alpha = 1 \times 10^{11}$ cm^{-2} V^{-1}. This is slightly larger than the lever arm estimated for a parallel plate capacitor model of 7.4×10^{10} cm^{-2} V^{-1} but in well agreement with an enhanced lever arm due to electrostatic fringe fields, which is also seen in a similar study on graphene ribbons.[17,34] Assuming $\nu = 2$, we approximate a constant contact resistance of 2450 Ω (see Figure S3, Supporting Information).

The region of suppressed conductance around $V_{BG} \approx 2$ V is also heavily influenced by the magnetic field (see Figure 2b). At $B = 0$ T, the region of suppressed conductance is dominated by statistical Coulomb blockade (see also Figure 2d). For increasing magnetic field, we still observe Coulomb peaks inside the gap region, while the average conductance increases, showing a maximum at around 2.5 T (see also Figure S4, Supporting Information). Above 2 T, a new region evolves where the conductance is completely suppressed and no Coulomb peaks can be observed at all. With further increase in the B-field, this region rapidly increases suppressing all conductance at 9 T from around $V_{BG} = 1$ V up to nearly $V_{BG} = 2.7$ V. In Figure 2d, we show the conductance as a function V_{BG} for different magnetic field values.

Similar measurements are also performed on the smaller (35 nm) nanoribbon device (see **Figure 3**a). The change in conductance with respect to the magnetic field becomes even more pronounced when averaging G in the regime of the suppressed transport. The range of BG voltage for the averaging is chosen by a linear approximation at 9 T similar to that described in section Device Characterization to approximate the maximum extent of the region of suppressed current. Figure 3b shows $\langle G \rangle$ from $V_{BG} = -1$ V to $V_{BG} = 4$ V as a function of the B-field for device D1. From $B = 0$ to slightly below 2 T, $\langle G \rangle$ increases by a factor of five due to i) an increase in the density of states around zero energy because of the formation of Landau levels and ii) due to an increase in the average mode transmission as, from a semi-classical point of view, straight trajectories ($B = 0$ T) are less likely to enter the nanoribbon than curved ones ($B > 0$ T). Between $B = 1.8$ and 2.8 T, $\langle G \rangle$ stays roughly constant, most likely because of smearing out the condition to enter the quantum Hall regime ($r_c(n) < w/2$, see the white dashed line in Figure 2a) due to charge carrier inhomogeneities. This is obviously most pronounced around the charge neutrality point, and the shifted
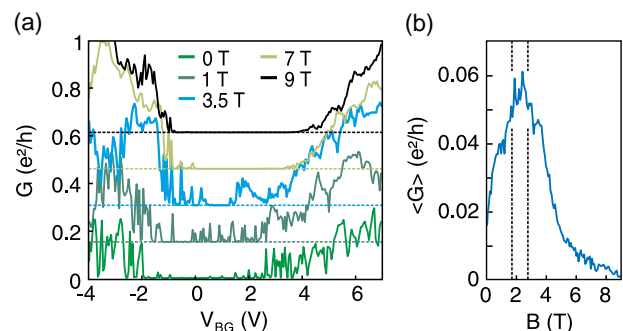

Figure 3. a) Conductance G as a function of V_{BG} for $B = 0$, 1, 3.5, 7, and 9 T between $V_{BG} = -4$ V and $V_{BG} = 6.5$ V. Each trace is offset by 0.15 $e^2\,h^{-1}$ for clarity. b) Averaged conductance $\langle G \rangle$ between $V_{BG} = -1$ and 4 V as a function of magnetic field. All data taken from device D1.

transition point to enter the quantum Hall regime for $n*$ between 1×10^{11} and $2 \times 10^{11}\,\mathrm{cm}^{-2}$ as indicated by the dashed lines in Figure 3b. Above $B = 3\,\mathrm{T}$, $\langle G \rangle$ decreases strongly. This suppression of transport with increasing magnetic field has already been seen in studies with high-mobility suspended graphene[13–15,17] or dual-gated graphene flakes supported on hBN[16] but, thus far, not on substrate-supported nanoribbons. To investigate the related energy gap in more detail, we performed bias spectroscopy measurements in dependency of the LG voltage V_{LG} for different magnetic fields. In **Figure 4**a, we show the differential conductance dI_{SD}/dV_{bias} at $B = 0\,\mathrm{T}$ as a function of V_{bias} and V_{LG} in the center of the transport gap at $V_{BG} = 1.5\,\mathrm{V}$, which shows the typical behavior of a nanoribbon dominated by statistical Coulomb blockade between $V_{LG} = -5\,\mathrm{V}$ and $V_{LG} = 2.5\,\mathrm{V}$. We determined an effective energy gap of $E_g \approx 14\,\mathrm{meV}$ (at $B = 0\,\mathrm{T}$) by estimating the maximum extent of suppressed current in bias voltage direction. The estimated E_g is a factor of two to three smaller than that reported for similar-sized nanoribbons on $\mathrm{SiO_2}$.[41,42] At 2.25 T (see Figure 4b), the effective energy gap is reduced considerably ($E_g \approx 6\,\mathrm{meV}$) due to the elevated transmission transparency. At 6 and 9 T (see Figure 4c,d), the statistical Coulomb blockade is strongly suppressed, and we observe extended regions of completely blocked transport between $V_{LG} = -3\,\mathrm{V}$ and $V_{LG} = 5\,\mathrm{V}$. The energy gap increases with magnetic field and exhibits a maximum of 20 meV at 9 T around the charge neutrality point of the nanoribbon (see the white dashed line). To investigate the B-field dependency in more detail, we performed finite-bias spectroscopy measurements as a function of the magnetic field (see **Figure 5**a) at $V_{LG} = -1\,\mathrm{V}$. Between $B = 0$ and 3.5 T, we observed statistical Coulomb blockade of a disordered system which gets suppressed with increasing magnetic field as the density of states increases with the magnetic field. Up to $B = 0.5\,\mathrm{T}$, the effective energy gap of the Coulomb blockade varies around 10 meV and a nonlinear I–V characteristic can be seen (see the blue trace in Figure 5b). When further increasing the B-field, E_g nearly shrinks to zero with an almost linear I–V characteristic (see 1T-trace in Figure 5b) consistent with the large increase in average conductance seen in Figure 3b. In contrast, between
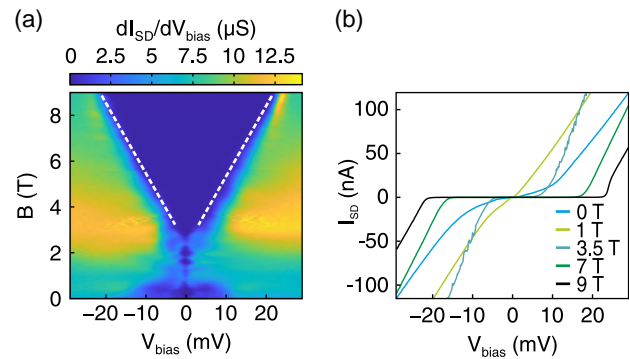

Figure 5. a) Finite-bias spectroscopy as a function of the B-field at $V_{BG} = 1.5\,\mathrm{V}$ and $V_{LG} = -1\,\mathrm{V}$. Between $B = 3.5$ and 9 T, a V-shaped insulating state with an energy gap increasing with roughly 3 meV T^{-1} up to 20 meV is visible. b) I–V characteristic at $B = 0$, 1, 3.5, 7, and 9 T. All data taken from device D1.

$B = 3.5$ and 9 T, we see a second type of energy gap, which increases with a slope of roughly 3 meV T^{-1} up to 20 meV at 9 T (see also high B-field traces in Figure 5b). A very similar behavior is seen in our wider nanoribbon (device D2) where the energy gap evolves roughly with a slope of 3.75 meV T^{-1} (see **Figure 6**).

Previous studies have proposed that the increasing magnetic field breaks the valley symmetry and opens up an electron–electron interaction-induced $\nu = 0$ energy gap.[14–16,43] Remarkably, in all studies, this $\nu = 0$ state scales linearly with magnetic field. Most simply, we can estimate the electron–electron interaction strength by the Coulomb energy $E_c = e^2/(\varepsilon_0 \varepsilon_r l_B)$,[15,16] where l_B is the magnetic length $l_B = \sqrt{(\hbar/eB)}$ and $\varepsilon_r = 4$ (due to hBN). Thus, E_c scales with $\sqrt{B}$ and cannot explain the observed linear dependence. However, considering valley symmetry breaking terms of higher order given by $\delta E_c = (a/l_B)E_c$,[15,16,43] where a is the carbon-carbon bond length, the observed linear dependency ($\delta E_c \propto B$) can be explained. Estimating this higher order contribution yields a gap of $\delta E_c \approx 1\,\mathrm{meV}\,\mathrm{T}^{-1}$.[16] For extended
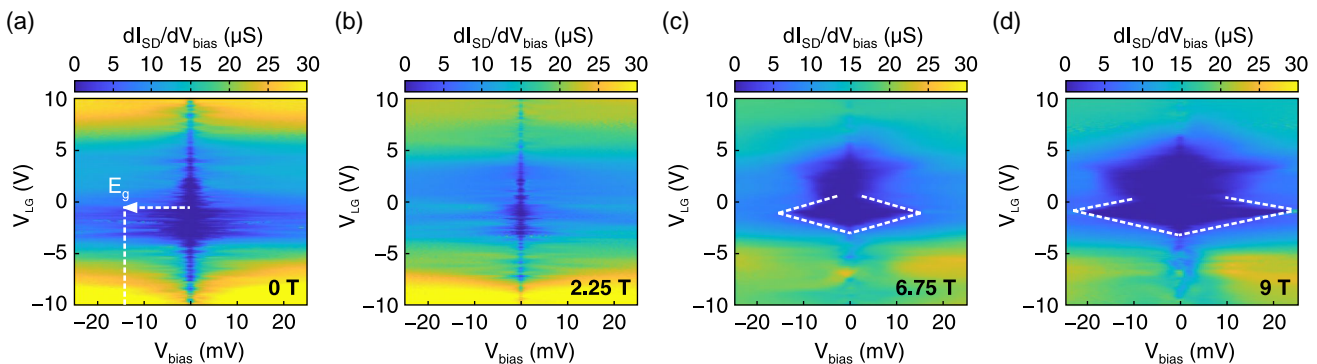

Figure 4. a) Finite-bias spectroscopy measurements at $B = 0\,\mathrm{T}$ as a function of V_{LG} in the center of the transport gap at $V_{BG} = 1.5\,\mathrm{V}$ exhibiting statistical Coulomb diamonds with charging energy E_g around 14 meV. b) Finite bias spectroscopy measurements at $B = 2.25\,\mathrm{T}$ still exhibiting statistical Coulomb diamonds with E_g around 6 meV. c) Finite-bias spectroscopy measurements at $B = 6.75\,\mathrm{T}$. An extended diamond-like feature indicated by the white dashed lines emerges around $V_{LG} = -1\,\mathrm{V}$ where all transport is suppressed. d) Finite-bias spectroscopy measurements at $B = 9\,\mathrm{T}$. The diamond-like feature increased with the increase in the magnetic field and exhibits a maximum of 20 meV. All data taken from device D1.

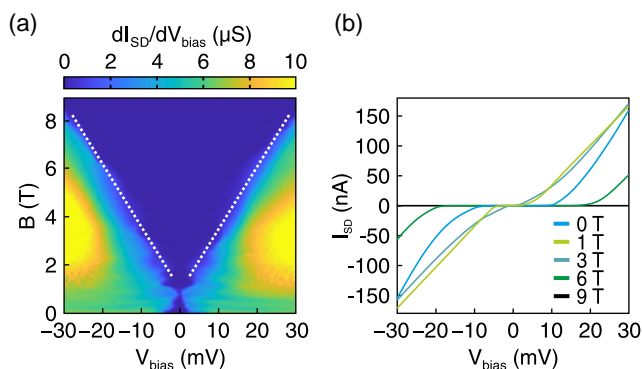**Figure 6.** a) Finite-bias spectroscopy as a function of B-field at $V_{BG} = 1.5$ V and $V_{LG} = 0$ V. Between $B = 2$ and 9 T, a V-shaped insulating state with an energy gap increasing with roughly 3.75 meV T^{-1} up to 30 meV is visible. b) I–V characteristic at $B = 0$, 1, 3, 6, and 9 T. All data taken from device D2.

graphene, this approximation shows good agreement with experimental values,[16] but it is roughly three to four times smaller than the value we extract for the graphene nanoribbon devices, indicating that size confinement effects play a crucial role. This is indeed likely as δE_c scales directly with the electron–electron interaction strength (E_c), which increases with an increased density of states when turning from a 2D electronic system to an effectively 1D system.

In summary, we present an investigation of encapsulated graphene nanoribbons with a width of around 35 and 40 nm. The measurements at zero magnetic field show disorder-dominated transport similar to that observed in nanoconstrictions on SiO$_2$ and hBN. However, our fully encapsulated devices exhibit a smaller transport and effective energy gap. Interestingly, the magnetotransport is similar to high-mobility suspended extended graphene sheets[13–15] and nanoconstrictions[17] or larger dual-gated graphene sheets on hBN.[16] At magnetic fields of around $B \approx 1$ T, we observe a crossover from the Coulomb blockade regime to a regime of elevated average conductance due to an increase in the density of states at zero energy as the electrons condense into Landau levels. At moderate magnetic fields of $B \approx 2.5$–3.5 T, the transport starts to be dominated by an energy gap due to electron–electron interaction, which completely prevents transport and the gap increases considerably with a slope of roughly 3 meV T^{-1} up to 20 meV and 3.75 meV T^{-1} up to 30 meV at 9 T for devices D1 and D2, respectively. The linear increase of this $\nu = 0$ energy gap points towards a valley symmetry breaking induced by the magnetic field. Compared to extended graphene on hBN,[16] our observed slope is a factor of three to four larger, potentially due to an enhancement of the electron–electron interaction due to the spatial confinement.

Supporting Information

Supporting Information is available from the Wiley Online Library or from the author.

Conflict of Interest

The authors declare no conflict of interest.

[1] K. Nakada, M. Fujita, G. Dresselhaus, M. S. Dresselhaus, *Phys. Rev. B* **1996**, *54*, 17954.
[2] L. Brey, H. A. Fertig, *Phys. Rev. B* **2006**, *73*, 235411.
[3] Y.-W. Son, M. L. Cohen, S. G. Louie, *Phys. Rev. Lett.* **2006**, *97*, 216803.
[4] S. Dutta, S. Lakshmi, S. K. Pati, *Phys. Rev. B* **2008**, *77*, 073412.
[5] A. A. Shylau, I. V. Zozoulenko, H. Xu, T. Heinzel, *Phys. Rev. B* **2010**, *82*, 121410(R).
[6] A. A. Shylau, I. V. Zozoulenko, *Phys. Rev. B* **2011**, *84*, 075407.
[7] V. N. Kotov, B. Uchoa, V. M. Pereira, F. Guinea, A. H. Castro Neto, *Rev. Mod. Phys.* **2012**, *84*, 1067.
[8] S. Ihnatsenka, G. Kirczenow, *Phys. Rev. B* **2013**, *88*, 125430.
[9] A. D. Güçlü, P. Grabowski, P. Hawrylak, *Phys. Rev. B* **2013**, *87*, 035435.
[10] S. S. Kahnoj, S. B. Touski, M. Pourfath, *Appl. Phys. Lett.* **2014**, *105*, 103502.
[11] C. R. Dean, L. Wang, P. Maher, C. Forsythe, F. Ghahari, Y. Gao, J. Katoch, M. Ishigami, P. Moon, M. Koshino, T. Taniguchi, K. Watanabe, K. L. Shepard, J. Hone, P. Kim, *Nature* **2013**, *497*, 598.
[12] L. A. Ponomarenko, R. V. Gorbachev, G. L. Yu, D. C. Elias, R. Jalil, A. A. Patel, A. Mishchenko, A. S. Mayorov, C. R. Woods, J. R. Wallbank, M. Mucha-Kruczynski, B. A. Piot, M. Potemski, I. V. Grigorieva, K. S. Novoselov, F. Guinea, V. I. Fal'ko, A. K. Geim, *Nature* **2013**, *497*, 594.
[13] X. Du, I. Skachko, F. Duerr, A. Luican, E. Y. Andrei, *Nature* **2009**, *462*, 192.
[14] K. I. Bolotin, F. Ghahari, M. D. Shulman, H. L. Stormer, P. Kim, *Nature* **2009**, *462*, 196.
[15] A. F. Young, C. R. Dean, L. Wang, H. Ren, P. Cadden-Zimansky, K. Watanabe, T. Taniguchi, J. Hone, K. L. Shepard, P. Kim, *Nat. Phys.* **2012**, *8*, 550.
[16] F. Amet, J. R. Williams, K. Watanabe, T. Taniguchi, D. Goldhaber-Gordon, *Phys. Rev. Lett.* **2013**, *110*, 216601.
[17] D.-K. Ki, A. F. Morpurgo, *Phys. Rev. Lett.* **2012**, *108*, 266601.
[18] J. Moser, A. Bachtold, *Appl. Phys. Lett.* **2009**, *95*, 173506.
[19] C. Stampfer, J. Güttinger, S. Hellmüller, F. Molitor, K. Ensslin, T. Ihn, *Phys. Rev. Lett.* **2009**, *102*, 056403.
[20] K. Todd, H.-T. Chou, S. Amasha, D. Goldhaber-Gordon, *Nano Lett.* **2009**, *9*, 416.

[21] X. Liu, J. B. Oostinga, A. F. Morpurgo, L. M. K. Vandersypen, *Phys. Rev. B* **2009**, *80*, 121407(R).

[22] P. Gallagher, K. Todd, D. Goldhaber-Gordon, *Phys. Rev. B* **2010**, *81*, 115409.

[23] J. B. Oostinga, B. Sacépé, M. F. Craciun, A. F. Morpurgo, *Phys. Rev. B* **2010**, *81*, 193408.

[24] M. Y. Han, J. C. Brant, P. Kim, *Phys. Rev. Lett.* **2010**, *104*, 056801.

[25] D. Bischoff, A. Varlet, P. Simonet, M. Eich, H. C. Overweg, T. Ihn, K. Ensslin, *Appl. Phys. Rev.* **2015**, *2*, 031301.

[26] C. R. Dean, A. F. Young, I. Meric, C. Lee, L. Wang, S. Sorgenfrei, K. Watanabe, T. Taniguchi, P. Kim, K. L. Shepard, J. Hone, *Nat. Nanotechnol.* **2010**, *5*, 722.

[27] J. Xue, J. Sanchez-Yamagishi, D. Bulmash, P. Jacquod, A. Deshpande, K. Watanabe, T. Taniguchi, P. Jarillo-Herrero, B. J. LeRoy, *Nat. Mater.* **2011**, *10*, 282.

[28] L. Wang, I. Meric, P. Y. Huang, Q. Gao, Y. Gao, H. Tran, T. Taniguchi, K. Watanabe, L. M. Campos, D. A. Muller, J. Guo, P. Kim, J. Hone, K. L. Shepard, C. R. Dean, *Science* **2013**, *342*, 614.

[29] G.-H. Lee, G.-H. Park, H.-J. Lee, *Nat. Phys.* **2015**, *11*, 925.

[30] I. V. Borzenets, F. Amet, C. T. Ke, A. W. Draelos, M. T. Wei, A. Seredinski, K. Watanabe, T. Taniguchi, Y. Bomze, M. Yamamoto, S. Tarucha, G. Finkelstein, *Phys. Rev. Lett.* **2016**, *117*, 237002.

[31] D. Bischoff, T. Krähenmann, S. Dröscher, M. A. Gruner, C. Barraud, T. Ihn, K. Ensslin, *Appl. Phys. Lett.* **2012**, *101*, 203103.

[32] S. Engels, A. Epping, C. Volk, S. Korte, B. Voigtländer, K. Watanabe, T. Taniguchi, S. Trellenkamp, C. Stampfer, *Appl. Phys. Lett.* **2013**, *103*, 073113.

[33] O. Herrmanna, C. Gould, L. W. Molenkamp, *J. Appl. Phys.* **2016**, *120*, 164304.

[34] B. Terrés, L. A. Chizhova, F. Libisch, J. Peiro, D. Jörger, S. Engels, A. Girschik, K. Watanabe, T. Taniguchi, S. V. Rotkin, J. Burgdörfer, C. Stampfer, *Nat. Commun.* **2016**, *7*, 11528.

[35] S. Somanchi, B. Terrés, J. Peiro, M. Staggenborg, K. Watanabe, T. Taniguchi, B. Beschoten, C. Stampfer, *Ann. Phys. (Berlin)* **2017**, *529*, 1700082.

[36] C. Neumann, S. Reichardt, P. Venezuela, M. Drögeler, L. Banszerus, M. Schmitz, K. Watanabe, T. Taniguchi, F. Mauri, B. Beschoten, S. V. Rotkin, C. Stampfer, *Nat. Commun.* **2015**, *6*, 8429.

[37] F. Forster, A. Molina-Sanchez, S. Engels, A. Epping, K. Watanabe, T. Taniguchi, L. Wirtz, C. Stampfer, *Phys. Rev. B* **2013**, *88*, 085419.

[38] J. Güttinger, C. Stampfer, F. Libisch, T. Frey, J. Burgdörfer, T. Ihn, K. Ensslin, *Phys. Rev. Lett.* **2009**, *103*, 046810.

[39] J. Güttinger, T. Frey, C. Stampfer, T. Ihn, K. Ensslin, *Phys. Rev. Lett.* **2010**, *105*, 116801.

[40] C. Volk, C. Neumann, S. Kazarski, S. Fringes, S. Engels, F. Haupt, A. Müller, C. Stampfer, *Nat. Commun.* **2013**, *4*, 1753.

[41] J. Dauber, B. Terrés, C. Volk, S. Trellenkamp, C. Stampfer, *Appl. Phys. Lett.* **2014**, *104*, 083105.

[42] F. Molitor, C. Stampfer, J. Güttinger, A. Jacobsen, T. Ihn, K. Ensslin, *Semicond. Sci. Technol.* **2010**, *25*, 034002.

[43] J. Alicea, M. P. A. Fisher, *Phys. Rev. B* **2006**, *74*, 075422.

[44] W. Albrecht, J. Moers, B. Hermanns, *J. Large-Scale Res. Facil.* **2017**, *3*, A112.

1900269 (6 of 6)